Revised Draft, 20110704
Preprint typeset using LaTeX style emulateapj v. 11/10/09

arXiv:1010.3017v2 [astro-ph.CO] 7 Jul 2011

EXTENDED LYMAN-ALPHA EMISSION AROUND STAR-FORMING GALAXIES

Zheng Zheng[1], Renyue Cen[2], David Weinberg[3], Hy Trac[4], and Jordi Miralda-Escudé[5,6]

Revised Draft, 20110704

ABSTRACT

Lyα photons that escape the interstellar medium of star-forming galaxies may be resonantly scattered by neutral hydrogen atoms in the circumgalactic and intergalactic media, thereby increasing the angular extent of the galaxy's Lyα emission. We present predictions of this extended, low surface brightness Lyα emission based on radiative transfer modeling in a cosmological reionization simulation. The extended emission can be detected from stacked narrowband images of Lyα emitters (LAEs) or of Lyman break galaxies (LBGs). Its average surface brightness profile has a central cusp, then flattens to an approximate plateau beginning at an inner characteristic scale below $\sim$0.2 Mpc (comoving), then steepens again beyond an outer characteristic scale of $\sim$ 1 Mpc. The inner scale marks the transition from scattered light of the central source to emission from clustered sources, while the outer scale marks the spatial extent of scattered emission from these clustered sources. Both scales tend to increase with halo mass, UV luminosity, and observed Lyα luminosity. The extended emission predicted by our simulation is already within reach of deep narrowband photometry using large ground-based telescopes. Such observations would test radiative transfer models of emission from LAEs and LBGs, and they would open a new window on the circumgalactic environment of high-redshift star-forming galaxies.

Subject headings: cosmology: observations — galaxies: halos — galaxies: high-redshift — galaxies: statistics — intergalactic medium — large-scale structure of universe — radiative transfer — scattering

1. INTRODUCTION

High-redshift star-forming galaxies are becoming an important probe of galaxy formation, reionization, and cosmology. Ionizing photons of young stars in star-forming galaxies ionize neutral hydrogen atoms in the interstellar medium (ISM), and each subsequent recombination has a probability of $\sim 2/3$ of ending up as a Lyα photon (Partridge & Peebles 1967). After escaping the ISM, these Lyα photons can be scattered by neutral hydrogen atoms in the circumgalactic and intergalactic media (IGM), which tends to make the Lyα emission extended. In this paper, we present predictions for the extended Lyα emission associated with high-redshift star-forming galaxies from a radiative transfer model of Lyα emission applied to a hydrodynamic cosmological simulation (Zheng et al. 2010).

As a result of reprocessed ionizing photons, prominent Lyα emission can be a characteristic of star-forming galaxies, which can be used to detect high-redshift galaxies. Galaxies detected through the strong Lyα emission associated with them (e.g., from narrowband photometry) are dubbed Lyman-alpha emitters (LAEs) and an increasing number of such galaxies have been discovered (e.g., Hu & McMahon 1996; Cowie & Hu 1998; Rhoads et al. 2003; Malhotra & Rhoads 2004; Gawiser et al. 2007; Ouchi et al. 2008; Guaita et al. 2010; Ouchi et al. 2010). High-redshift star-forming galaxies can also be detected from broadband photometry with Lyman break technique, which are termed Lyman break galaxies (LBGs; e.g., Steidel et al. 2003). As long as Lyα photons reprocessed from ionizing photons can escape from the ISM, Lyα emission is also expected to be associated with LBGs. Lyα emission encodes useful information about star-forming galaxies and their environments, such as star formation rate (e.g., Madau et al. 1998), kinematics of ISM gas (e.g., Steidel et al. 2010), and neutral fraction of IGM gas (e.g., Dijkstra et al. 2007). Lyα photons usually experience complex radiative transfer processing (resonant scatterings) in media with neutral hydrogen atoms, which complicates the interpretation of observed Lyα emission properties.

Zheng et al. (2010) (hereafter Paper I) present a physical model of Lyα emission from LAEs by solving Lyα radiative transfer in the circumgalactic and intergalactic media. The Lyα radiative transfer calculation is performed in a cosmological volume ($100h^{-1}$Mpc on a side) from a state-of-the-art radiation-hydrodynamic reionization simulation (Trac et al. 2008). The calculation uses a 768^3 grid to sample the density, velocity, and temperature of the neutral hydrogen gas in the simulation and is applied to all the sources residing in halos above $5 \times 10^9 h^{-1} M_\odot$. Resonant scatterings enable Lyα photons to probe the circumgalactic and intergalactic environments (density and velocity structures) around star-forming galaxies. This leads to a coupling between the observed Lyα emission properties and the environments. This simple physical model is able to explain an array of observed properties of $z \sim$5.7 LAEs the Subaru/*XMM*-

---

[1] Yale Center For Astronomy and Astrophysics, Yale University, New Haven, CT 06520; zheng.zheng@yale.edu
[2] Department of Astrophysical Sciences, Princeton University, Peyton Hall, Ivy Lane, Princeton, NJ 08544
[3] Department of Astronomy, Ohio State University, Columbus, OH 43210
[4] Department of Physics, Carnegie Mellon University, Pittsburgh, PA 15213
[5] Institució Catalana de Recerca i Estudis Avançats, Barcelona, Catalonia
[6] Institut de Ciències del Cosmos, Universitat de Barcelona, Barcelona, Catalonia

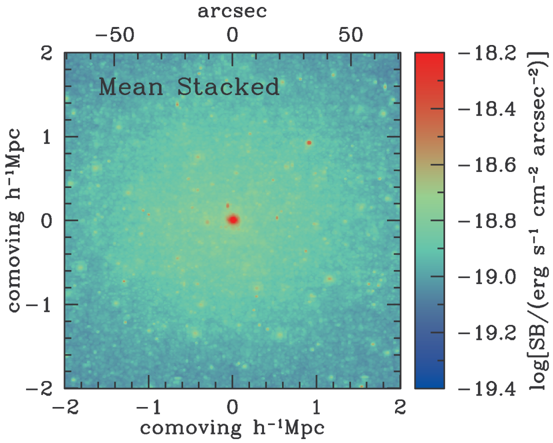

FIG. 1.— Stacked narrowband Lyα image for sources residing in halos of $10^{11}h^{-1}M_{\odot}$ at $z\sim$5.7. A mean algorithm is used to stack $\sim$440 sources.

Newton Deep Survey (SXDS; Ouchi et al. 2008), including Lyα spectra, morphology, apparent Lyα luminosity function (LF), shape of the ultraviolet (UV) LF, and the distribution of Lyα equivalent width. The selection imposed by the environment dependent radiative transfer also introduces interesting new features in the clustering of LAEs (Zheng et al. 2011, hereafter Paper II).

In the above radiative transfer model, while the number of Lyα photons is conserved after they escape the ISM, the scatterings in the circumgalactic and intergalactic media cause the Lyα emission to spread spatially. Therefore, one generic prediction of the model is an extended Lyα emission halo around a star-forming galaxy. Observationally, only a fraction of Lyα photons can be detected for an individual source, those included in the central part of the extended Lyα emission with high enough surface brightness (tip of the iceberg). The outskirts of the Lyα halo with low surface brightness is typically buried in the sky noise.

In this paper, we show that it is possible to detect the bottom of the iceberg by stacking the narrowband images of a large number of sources to suppress the sky noise. We present the predictions of the extended Lyα emission in the stacked image from our radiative transfer model and discuss what we can learn from it. Our radiative transfer modeling is performed for sources at $z\sim 5.7$. We study properties of Lyα surface brightness profile from stacked images in Section 2. In Section 3, we discuss the observational prospects. We summarize our results in Section 4.

Throughout the paper, we adopt a spatially flat ΛCDM cosmological model for our calculations, with a matter density parameter $\Omega_m = 0.28$ and a Hubble constant $h = 0.70$ in units of $100\,\mathrm{km\,s^{-1}Mpc^{-1}}$. Distances are expressed in comoving units unless mentioned clearly otherwise.

2. EXTENDED Lyα EMISSION AROUND STAR-FORMING GALAXIES

The Lyα radiative transfer calculation in Paper I is performed in a simulation box of $100h^{-1}$Mpc (comoving) on a side with the neutral hydrogen density, temperature, and peculiar velocity sampled with a 768^3 grid. The cell size is therefore $130.2h^{-1}$kpc (comoving), about the virial diameter of a $1.8\times10^{10}h^{-1}M_{\odot}$ halo. The star-forming region in a high-redshift galaxy, where Lyα photons in our study originate, is only a few kpc (comoving) across (e.g., Taniguchi et al. 2009). So the initial Lyα emission is treated as a point source at the halo center for the purpose of the radiative transfer calculation. The size of the pixel for collecting Lyα photons is 8 times finer, corresponding to $16.3h^{-1}$kpc (comoving) or $0.58''$. With the cell resolution, the gas distribution is uniform inside the virial radius of small halos (below a few times $10^{10}h^{-1}M_{\odot}$), which would have some effect on the Lyα surface brightness profile. However, since Lyα photons are initially emitted from a point source and the dynamics of the infall region around halos plays a significant role in determining the distribution of Lyα photons (Paper I), the resolution we use is sufficient for obtaining the generic features in the extended Lyα emission. We present a resolution test in § 2.5, and the main results presented in this paper would remain valid with improved resolution. Our calculation does not address the effects of galactic wind and dust, and we discuss these model uncertainties in § 2.4 and § 3.

2.1. *Stacked Lyα Image and Lyα Emission at Fixed Halo Mass*

We start from the stacked Lyα image for sources residing in halos of fixed mass, $10^{11}h^{-1}M_{\odot}$. In our model, the intrinsic Lyα luminosity, which is the the total amount of Lyα emission from the reprocessed ionizing photons, is tightly correlated with the halo mass, therefore this stacking is basically for sources at fixed intrinsic Lyα luminosity or UV luminosity.

Our radiative transfer model produces a three-dimensional array, recording the Lyα spectra as a function of spatial position on the sky. We construct the narrowband Lyα image from this array, with a filter width similar to that in the $z\sim 5.7$ SXDS (see Paper I). Our simulation box has about the same area as SXDS with a redshift depth three times larger. So we are able to construct narrowband Lyα images for three SXDS-like fields. Each image corresponds to an ideal case with perfect continuum and sky subtraction. Examples of images of individual sources can be found in Paper I (Fig.4 and Fig.5). We stack all the source images together as would be done with the narrowband observation. For each source, the image includes the center and surrounding pixels (up to a radius of $\sim 10h^{-1}$Mpc). The center pixel is chosen to be the one that contains the halo center. In other words, the center corresponds to that in the UV band. It is evident that the surrounding pixels can include Lyα photons from other neighboring sources. For all the sources in a narrow bin (0.16 dex) of halo mass around $10^{11}h^{-1}M_{\odot}$ (about 440 sources for each of the SXDS-like fields), we stack their images with their centers aligned.

Typically there are two algorithms to generate a stacked image, taking either the mean or the median. The stacked Lyα image from the mean algorithm is shown in Figure 1. The mean algorithm has the advantage of conserving the flux, even though it may be affected by outliers in the flux distribution, showing up as many small clumps in the stacked image. The median stacked image has the advantage of insensitivity to outliers. We find that at a fixed projected radius, the observed flux roughly follows a log-normal distribution among different sources, which causes the surface brightness from the median stacked image to be lower in amplitude than that from the mean stacked image (see solid curves in Figure 2). The stacking cases mentioned above correspond to an ideal situation of no photon noise. When total photon noise (source + sky) is added, the surface brightness profile from the mean stacked image remains the same and that from the median stacked image would change. In the limit of large noise (compared to the signal distribution), the flux distribution is completely modified by the noise distribution, and the median value is driven to be close to the mean (also see Pieri et al. 2010). In practice, the large noise limit is typical at large radii for the case considered here (see below), so the surface brightness profile from the median stacked image approaches that from the mean stacked one. See the thin solid curve in Figure 2. In what follows, we focus on presenting our results from the mean stacked image. We compute the surface brightness profile by averaging the flux in annuli at different radii, therefore the effect of the grainy feature seen in the image is greatly reduced.

The surface brightness profile from the stacked image shows a few interesting features. It has two characteristic scales that are associated with steep changes in the profile slope. The inner slope change occurs at $R_{\rm in} \sim 0.1h^{-1}$Mpc (possibly upper limit, see § 2.5) and the outer one at $R_{\rm out} \sim 1h^{-1}$Mpc. Inside the inner characteristic radius $R_{\rm in}$, the profile appears as a central cusp, roughly following a steep power-law. Between the inner and outer characteristic radii, $R_{\rm in} < R < R_{\rm out}$, the surface brightness decreases slowly with increasing radius, close to a plateau. Beyond the outer characteristic radius $R_{\rm out}$, the surface brightness profile steepens and drops, forming an extended tail. As shown later, the two scales have clear physical meanings.

With the mean surface brightness profile, we compute the cumulative luminosity as a function of projected radius (bottom panel of Figure 2). It turns out that the luminosity from the stacked image does not converge at large radius. Because of the plateau in the surface brightness profile, the luminosity profile approximately follows R^2, a trend similar to that from the global mean surface brightness (dot-dashed line). The global mean profile is computed by uniformly distributing the total Lyα flux in the original narrowband image across the whole image. The plateau in the stacked surface brightness profile has a much higher amplitude than the global mean. As we show later, the higher signal is caused by the clustered neighboring sources.

In the top panel of Figure 2, we also show the level of sky noise (dotted lines). The calculation is based on a 4-hour observation with the NB816 filter using the Subaru telescope[7], which is roughly the setup for the survey of $z \sim 5.7$ LAEs in SXDS (Ouchi et al. 2008). In the NB816 band, the sky (AB magnitude of 20.4mag/arcsec^2 in a dark night) has a surface brightness of $f_{\rm sky} \sim 1.36\times10^{-15}{\rm erg\,s^{-1}\,cm^{-2}\,arcsec^{-2}}$. The mean sky photon count in a 2″diameter aperture from a 4-hour exposure with the Subaru telescope reaches $N_{\rm sky} \sim 7.1\times10^6$. Therefore, the 1σ sky noise in a 2″diameter aperture corresponds to a surface brightness level of $f_{\rm sky}/\sqrt{N_{\rm sky}} \sim 5.1\times10^{-19}{\rm erg\,s^{-1}\,cm^{-2}\,arcsec^{-2}}$, which is higher than the signal of interest on large scales (Fig. 2). The noise per pixel is expected to be suppressed by $\sqrt{N}$ with N sources stacked. The suppression works even better for detecting the signal at large radii, because the annuli used to compute the mean surface brightness profile can be much larger than the 2″aperture. Within each annulus, however, the noise in different pixels is correlated, since the same pixel from the original image may fall into the annulus several times from centering different sources. The correlations need to be accounted for in estimating the noise level at each radius for the stacked profile. In practice, given the low surface brightness of the extended Lyα emission and the high sky noise level, stacking the image before subtracting the continuum and sky may help to reduce errors caused by such subtraction and to increase the sensitivity.

2.2. *Decomposition of the Lyα Surface Brightness Profile in the Stacked Image*

To understand the features in the stacked Lyα surface brightness profile and the origin of the two characteristic scales, we perform a test by assigning artificial surface brightness profiles for individual sources. The image of each source (in halos above $5\times10^9h^{-1}M_\odot$) is assumed to be a circular disk of radius R_s with uniform surface brightness normalized such that the total luminosity is the intrinsic Lyα luminosity from the source. That is, we replace the intrinsic point source with a uniform "seeing" disk or (equivalently) modify it by a tophat point spread function (PSF). We then follow the same procedure as above to form the stacked image for sources in $10^{11}h^{-1}M_\odot$ halos and derive the Lyα surface brightness profile. No radiative transfer is performed in this artificial model, and we use it to illustrate the effect of source extent combined with source clustering.

Figure 3 shows the series of surface brightness profiles with different "seeing" disk radii R_s. For a small "seeing" disk radius ($R_s = 0.08h^{-1}$Mpc), sources are close to point-like. The central spike (inside R_s) is clearly seen in the profile from the stacked image. Outside of this radius, we still see signals, which are obviously contributed from neighboring sources as a result of clustering.

The surface brightness profile has contributions from the central sources and from the neighboring clustered sources, analogous to the case of weak gravitational lensing around galaxies. In the spirit of the halo model (e.g., Seljak 2000; Berlind & Weinberg 2002; Cooray & Sheth 2002), the profile can be decomposed into two components, that from the individual source (the one-halo term) and that caused by the clustering (the two-halo term). Formally, we can write the "two-halo" term of the stacked surface brightness profile $\Sigma_{\rm 2h}(\mathbf{R})$ as

$$\Sigma_{\rm 2h}(\mathbf{R}|M) = \int dM' \frac{dN}{dM'} \int d^2\mathbf{R}' \, [1+w(\mathbf{R}'|M,M')]\,\Sigma_{\rm 1h}(\mathbf{R}-\mathbf{R}'|M'), \quad (1)$$

where dN/dM' is the surface number density of halos, w is the 2D two-point correlation function (essentially

---

[7] We use the Subaru Imaging Exposure Time Calculator at http://www.naoj.org/cgi-bin/img_etc.cgi.

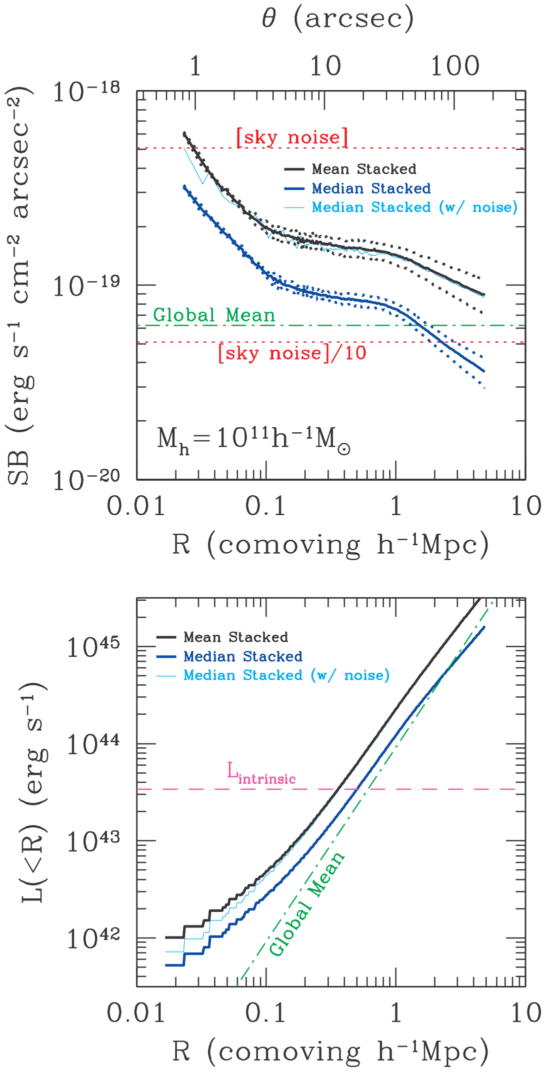

FIG. 2.— Surface brightness profile of extended Lyα emission from stacked narrowband image for sources residing in halos of $10^{11}h^{-1}M_\odot$. Top panel: the two thick solid curves are from mean and median stacked noise-free images, respectively. The associated dotted curves indicate the scatter around the mean surface brightness, based on stacked images from three SXDS-like fields in our model. The thin solid curve is from the *median* stacked noise-added images, where the Poisson photon noise (source + sky) is computed for a 4-hour exposure with the Subaru telescope. The upper horizontal dotted line is the surface brightness level corresponding to the 1σ sky noise in a 2$''$ diameter aperture, assuming a 4-hour exposure with the Subaru telescope. It drops to the lower horizontal dotted line if 100 sources are stacked. The horizontal dot-dashed line is the global mean Lyα surface brightness if the Lyα flux from all the sources in each field is uniformly distributed across the field. Bottom panel: The cumulative Lyα luminosity distributions from the stacked images. The dashed line denotes the intrinsic Lyα luminosity of one source residing in a halo of $10^{11}h^{-1}M_\odot$. The dot-dashed line is the profile from the global mean surface brightness profile, which is $\propto R^2$.

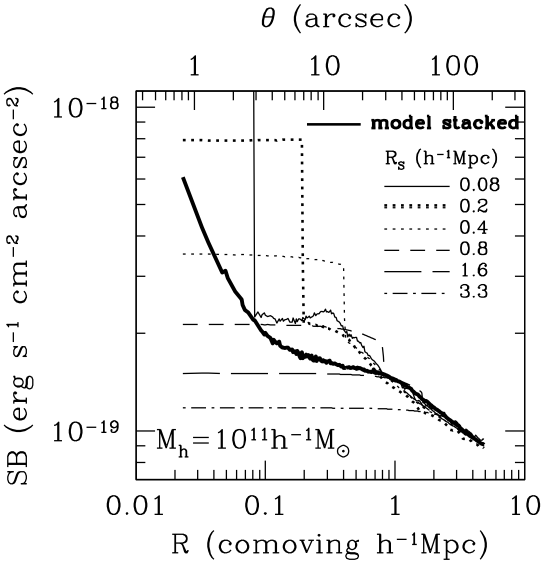

FIG. 3.— Lyα surface brightness profile from (mean) stacked images with different assumptions about the extent of Lyα emission. Sources considered here reside in halos of $10^{11}h^{-1}M_\odot$. The thick solid curve is the prediction from the radiative transfer model, which is the same as that in Fig. 2. Other curves are for cases with no radiative transfer applied but with the Lyα emission from a source artificially set to spread into a uniform "seeing" disk of radius R_s, which are to illustrate the effect of source extent combined with source clustering. The signal outside of this radius comes from the neighboring sources as a consequence of clustering. See the text.

the angular correlation function), and $\Sigma_{1\mathrm{h}}$ is the surface brightness profile of individual sources (the one-halo term). For simplicity, equation (1) assumes that $\Sigma_{1\mathrm{h}}$ depends only on halo mass, while in reality it depends on the environment around halos as well (see below). We emphasize that the one-halo term in the stacked profile is defined as the Lyα emission from the central source alone (i.e., contributed from all the sources to be center-aligned and stacked). Even though neighboring sources can have their Lyα photons scattered into the one-halo scales of the central source, these photons still belong to the contribution from the two-halo term.

In the limit of compact sources (small R_s in the uniform "seeing" disk case), $\Sigma_{1\mathrm{h}}$ can be replaced with $L(M')\delta_D(\mathbf{R}-\mathbf{R}')$, where $L(M')$ is the intrinsic Lyα luminosity and δ_D is the Dirac delta function. The two-halo term then becomes

$$\Sigma_{2\mathrm{h}}(R|M) = \int dM' \frac{dN}{dM'} L(M') \left[1 + w(R|M,M')\right]. \quad (2)$$

For the small "seeing" disk case in Figure 3 ($R_s = 0.08h^{-1}$Mpc), the flattening below $0.3h^{-1}$Mpc is a sign of the halo exclusion effect, which leads to a zero signal in the 3D two-point correlation function and a constant in the angular two-point correlation function w.[8]

According to Equation (2), we expect to see a flattened profile on large scales, where $w \ll 1$. On these scales, which are out of the range of the plot, it is hard in practice to disentangle such a uniform background from the sky background. We therefore limit ourselves to the regime where w is still large.

---

[8] The bump around $0.3h^{-1}$Mpc can be understood as follows. Roughly speaking, $w(R) \propto \int_{Z_0}^{\infty} \xi(R,Z)dZ$ with $Z_0 = \sqrt{r_c^2 - R^2}$ in the regime that $R < r_c$, where $r_c \sim 0.2$–$0.3h^{-1}$Mpc is the halo exclusion scale and ξ is the 3D two-point correlation function (zero on scales below r_c). As R increases, the competition between a decreasing ξ on average and an increasing path length of integration (i.e., a decreasing lower limit Z_0) leads to a small bump in w around $0.3h^{-1}$Mpc. If the seeing disk is comparable or larger than the size of the halo (e,g., the $R_s = 0.2h^{-1}$Mpc case in Figure 3 for $10^{11}h^{-1}M_\odot$ halos), the bump is smeared out.

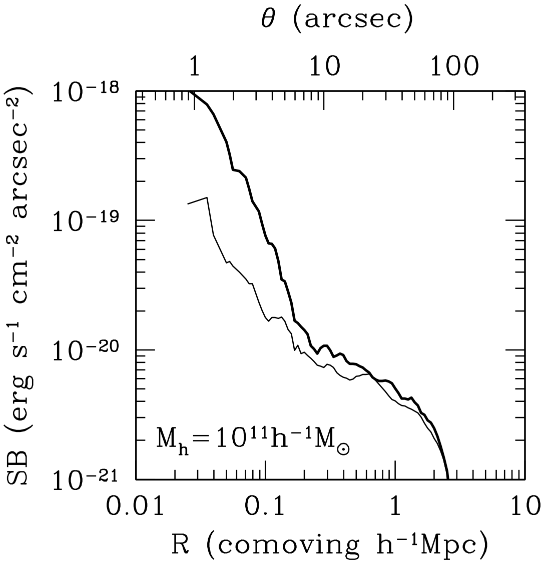

Fig. 4.— Mean Lyα surface brightness profile from an individual source. The host halo mass for this source is $10^{11}h^{-1}M_\odot$. The thick and thin curves are the same source viewed along different directions.

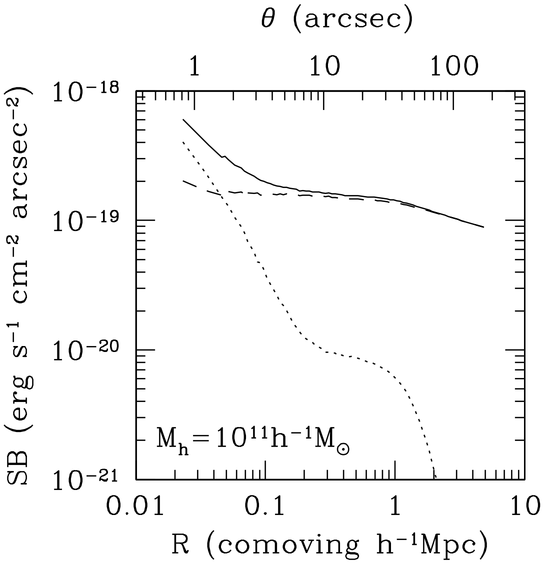

Fig. 5.— One-halo and two-halo contributions to the Lyα surface brightness profile. The dotted curve is the average profile from individual sources (one-halo term), and the dashed curve is the profile from source clustering (two-halo term). The solid curve is the sum of the two contributions, which would be the one from the stacked image.

By varying the radius R_s of the uniform "seeing" disk, we show the effect of the spatial extent of the Lyα emission on the surface brightness profile from the stacked image (Figure 3). As the "seeing" disk size increases, the two-halo term of the profile is smoothed on scales below the "seeing" disk size, which results in a decrease in the amplitude. In our setup, the uniform "seeing" disk has a surface brightness of $1.4 \times 10^{-19}(R_s/0.4h^{-1}\mathrm{Mpc})^{-2}\mathrm{erg\,s^{-1}\,cm^{-2}\,arcsec^{-2}}$ for $R < R_s$, which is by definition the one-halo term contribution. However, the small-scale surface brightness (in the one-halo regime) in Figure 3 decreases much slower than R_s^{-2}, as a consequence of the contribution from the smoothed two-halo term. For $R_s = 1.6h^{-1}$Mpc, the signal is already dominated by the two-halo term on all scales. The approximate plateau seen in the stacked profile from the radiative transfer model (thick solid curve) is close to the case with a "seeing" disk size of $R_s = 1.6h^{-1}$Mpc. The test suggests that the plateau feature between the two characteristic scales mainly originates from spatially extended, scattered Lyα emission from clustered sources around the central source.

The uniform "seeing" disk only gives us a rough idea on the features in the extended Lyα emission. To be more accurate, we need to examine the Lyα surface brightness profile of individual sources.

As an example, we show in Figure 4 the surface brightness profiles of one individual source in the simulation box from the radiative transfer model. The two curves correspond to the profiles viewed along different directions, and the difference reflects the environment dependent Lyα radiative transfer, as discussed in detail in Paper I. The surface brightness has a steep drop below $0.3h^{-1}$Mpc. Then it levels off until a cutoff is reached around 2–$3h^{-1}$Mpc. The inner surface brightness profile of one source roughly goes as R^{-2} and the luminosity increases logarithmically with radius. Most of the luminosity comes from near the cutoff radius at $\sim 2h^{-1}$Mpc, which is the reason why the plateau up to such a scale in the total profile is produced (see below).

As discussed in Paper I, the shape of the surface brightness profile largely depends on the velocity field. Below $0.3h^{-1}$Mpc, the contribution to the surface brightness profile mainly comes from the Lyα photons that are last scattered in the infall region around the halo. On larger scales, where the profile levels off, the last scattering of Lyα photons occurs in the IGM that undergoes Hubble flow. The cutoff radius corresponds to those photons that are the bluest after escaping the infall region. They can travel far away from the source before being redshifted into the line center to be significantly scattered in the IGM. The exact shape of the surface brightness profile also depends on the initial frequency of Lyα photons (see § 2.4).

As emphasized in Paper I and Paper II, Lyα radiative transfer depends on circumgalactic and intergalactic environments (density and velocity structures). Even for sources in halos of the same mass, there is a broad distribution of environments. Therefore, the one-halo term of the surface brightness profile is not identical for sources in halos of fixed mass or for the same source viewed along different directions (Figure 4). The one-halo term in Equation (1) should have dependence on environment in addition to halo mass. To obtain the mean one-halo term for the stacked image and decompose the surface brightness profile, we perform Lyα radiative transfer calculations separately for each source with halo mass in the $10^{11}h^{-1}M_\odot$ mass bin. We then stack the individual one-halo terms to obtain the mean.

The dotted curve in Figure 5 is the mean one-halo term for sources in $10^{11}h^{-1}M_\odot$ halos. The shape is similar to that seen in Figure 4. The dashed curve is the two-halo term, inferred from subtracting the one-halo term from the total surface brightness profile. The two-halo term can be expressed as a convolution (Equation 1), with the convolution kernel being the one-halo term of the

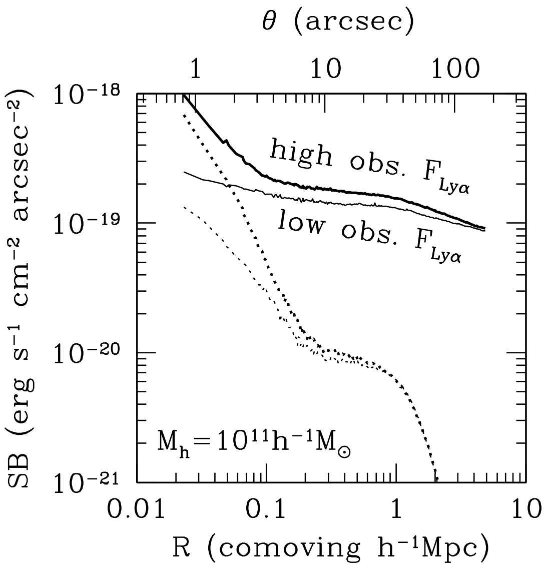

FIG. 6.— Surface brightness profile of extended Lyα emission from stacked narrowband image as a function of observed Lyα luminosity. All sources reside in halos of $10^{11}h^{-1}M_\odot$. Thin (thick) curves are for the faint (bright) half of the sources based on the observed Lyα luminosity, which is contributed by the central, high surface brightness region. Dotted curves are the corresponding one-halo profiles. See the text for details.

clustered star-forming halos of *all* masses. The shape of the one-halo term at different halo mass is similar to that shown in Figure 5. In the two-halo term, a plateau reaches out to a radius of 1–2h^{-1}Mpc, which is around the cutoff scale of the mass-averaged one-halo term. This is not a coincidence. The scale where the plateau in the two-halo term ends marks the spatial extent of the extended Lyα emission of the clustered sources, since on scales larger than this the smoothing effect from the source PSF is small. As the two-halo term dominates on large scales, the above scale is just the outer characteristic scale $R_{\rm out}$ seen in the total surface brightness profile. The inner characteristic scale $R_{\rm in}$ marks the transition from the one-halo term dominated regime to the two-halo term dominated regime. The realistic decomposition of the surface brightness profile confirms the results of the test in Figure 3 that the origin of the plateau between the two characteristic scales in the total surface brightness profile is the extended Lyα emission.

The environment dependent Lyα radiative transfer couples the observed Lyα emission with the circumgalactic and intergalactic environments. Many consequences of such a coupling are studied in Paper I and Paper II. For the stacked surface brightness profile, the environment dependence also appears, as detailed below.

At fixed halo mass, which corresponds to fixed intrinsic Lyα luminosity or UV luminosity in our model, the observed Lyα luminosity has a broad distribution, reflecting the distribution of environments. In our model, for each source we link together the pixels above a surface brightness threshold similar to that used in Ouchi et al. (2008) to define the observed emission, and if none of the pixels around the central source exceeds the threshold, we simply take the flux in the pixel at the source position as the observed emission (see Paper I for details). The observed luminosity is only a fraction of the extended Lyα emission, coming from the central, high surface brightness part of the source. The one-halo term of the surface brightness profile is expected to be closely related to the environment.

We divide the sources into two samples of equal size, according to the observed Lyα luminosity. In Figure 6, we show the stacked surface brightness profile for the bright half and faint half, respectively. The dotted curves show the corresponding one-halo terms. We note that the fluxes inferred from the one-halo terms of the two cases are not necessarily the same. The reason is that the scattered emission is not isotropic, being sensitive to the density and velocity structures around the source. Overall, the sample of sources with lower observed Lyα luminosity has a shallower stacked surface brightness profile at small radius and there is no clear scale of the transition from the inner cusp to the approximate plateau. The result implies that the stacked Lyα narrowband image for star-forming galaxies with weaker observed Lyα emission would appear to be less compact.

2.3. *Dependence on UV and Lyα Luminosity*

So far we have focused on the Lyα surface brightness profile for sources in halos of $10^{11}h^{-1}M_\odot$. The profile is expected to be a function of the halo mass. We show the dependence on halo mass in Figure 7, both for halo in narrow mass bins (left panel) and above different mass thresholds (right panel). Since in our model the UV luminosity is tightly correlated with halo mass, the plot also represents a sequence of Lyα profiles as a function of UV luminosity.

The amplitude of the stacked profile increases with halo mass. On small scales this increase is largely a reflection of the fact that halos of higher masses host sources of higher Lyα luminosity, while on large scales there is an additional contribution from stronger source clustering around more massive halos.

On small scales (inside the inner characteristic radius), where the one-halo profile makes a substantial contribution, sources in higher mass halos show a steeper profile. The inner characteristic scale $R_{\rm in}$, where the profile starts to level off, increases with halo mass. It implies that sources in higher mass halos have more extended Lyα emission. The outer characteristic scale $R_{\rm out}$, where the profile starts to steepen again, also increases with halo mass. As discussed above, this scale is an indication of the spatial extent of the Lyα emission of the clustered sources. Massive halos are typically located in dense environments, therefore the clustered sources around them tend to be in massive halos as well. On scales larger than $R_{\rm out}$, the extended tail of the profile for higher mass halos is steeper. This is also a consequence of the higher clustering amplitude, since the surface brightness profile is proportional to $(1+w)$ as in Equation (1), and the unity factor tends to flatten the profile for weakly clustered sources.

Overall, the stacked Lyα surface brightness profile is steeper for sources in higher mass halos, and the two characteristic scales increase with halo mass. On small scales where the central cusp dominates, if we approximate the profile by a power law, we find that the power-law index decreases with halo mass, ranging from -0.5 to -1.4 (from -0.5 to -1.7) for the mass bin (threshold) samples shown in Figure 7.

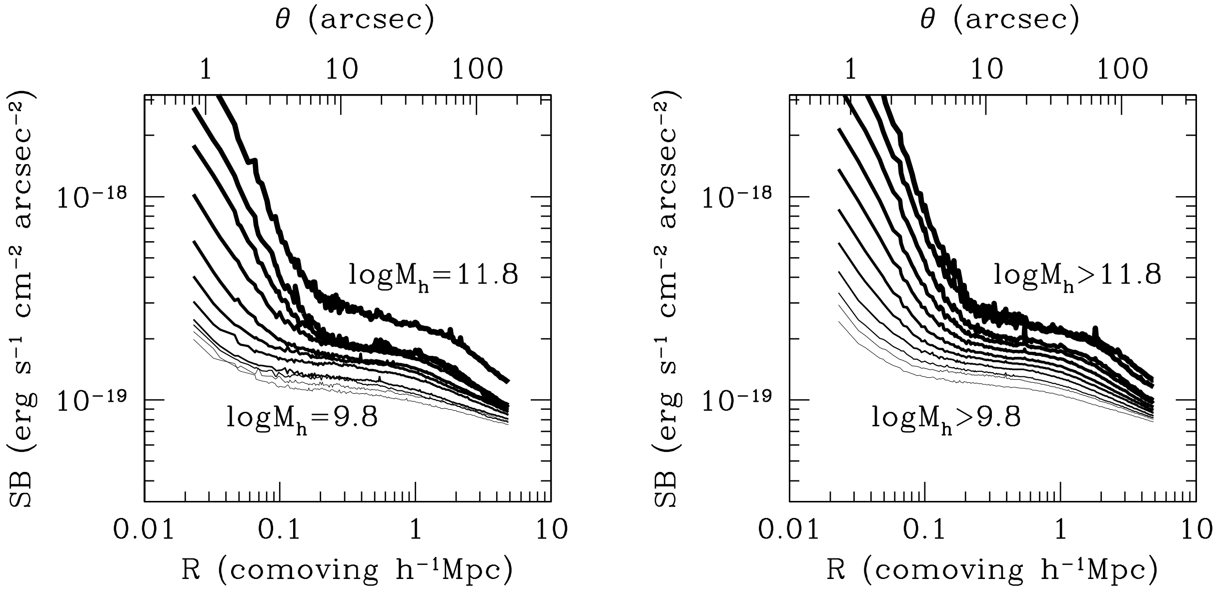

FIG. 7.— Dependence of mean Lyα surface brightness profile on host halo mass (or UV luminosity). *Left:* Profiles for samples of galaxies in different bins of halo mass. From bottom to top curves, host halo mass increases from $\log[M/h^{-1}M_\odot] = 9.8$ to 11.8, with an interval of 0.2 dex between two adjacent curves. *Right:* Similar to the left panel, but for samples of galaxies in halos above different mass thresholds.

The halo mass (UV luminosity) sequence does not have a priori selection based on observed Lyα emission, so it applies to the case of LBGs.

In practice, the brightness profile that can be easily measured in a narrowband survey is the stacked image of the identified LAEs, classified according to their apparent (observed) Lyα flux. Figure 8 shows the stacked Lyα surface brightness profile for LAEs as a sequence of the apparent (observed) Lyα luminosity, for both luminosity-bin samples (left panel) and luminosity-threshold samples (right panel).

The apparent Lyα luminosity couples to the circumgalactic and intergalactic environment around sources as a result of the Lyα radiative transfer, which imposes a strong selection effect for sources that are identified as LAEs. On small scales (inside $R_{\rm in}$), the stacked profile for LAEs appears to be steeper than those seen in cases in Figure 7 for sources without Lyα selection. In Figure 8, the central cuspy profile has a slope of $-0.9 - -1.8$ (-1.1 – -1.8) for luminosity bin (threshold) samples, with steeper slopes for higher observed Lyα luminosities. The amplitude increases with the apparent Lyα luminosity. On scales above the inner characteristic scale, the amplitude also increases with Lyα luminosity, but the dependence is much weaker. This weak dependence is a consequence of the weak dependence of the projected clustering on apparent Lyα luminosity, as discussed in Paper II. There is also a trend that the two characteristic scales increase with the apparent Lyα luminosity, but it is much weaker than that seen in Figure 7 for LBGs.

2.4. *Dependence on the Intrinsic Lyα Line Profile*

In all our discussions above, the intrinsic Lyα line profile is assumed to be Gaussian with the width determined by velocity dispersion in the halo (Paper I). More specifically, the standard deviation of the Gaussian profile is set to equal the 1D thermal velocity dispersion for gas in the halo, $\sigma = 31.9[M_h/(10^{10}h^{-1}M_\odot)]^{1/3}{\rm km\,s^{-1}}$. As discussed in Paper I and Paper II, the intrinsic line profile is one of the main uncertainties in our radiative transfer modeling. The spatial extent of the Lyα emission depends on the initial line profile. For example, in the extreme case where all the Lyα photons are shifted far to the red from the line center within the emitting galaxy (e.g., as a possible consequence of a strong galactic wind; Dijkstra & Wyithe 2010), they would not be further scattered in the surrounding medium and the Lyα emission would not extend beyond the size of the galaxy.

To test the effect of the initial line profile on the spatial distribution of Lyα photons, we perform radiative transfer calculations with different initial values of Lyα wavelength for an individual source in a halo of $10^{11}h^{-1}M_\odot$ (the same source as in Figure 4). Figure 9 shows the Lyα surface brightness and cumulative luminosity profiles for cases with different initial line shifts (in units of the thermal velocity dispersion σ mentioned above).

On average, bluer photons travel farther in the IGM before they redshift into the line center to encounter significant scatterings. Therefore, the Lyα emission would dilute to a larger spatial extent. This is clearly seen in Figure 9 – the spatial distribution becomes more and more extended as the initial Lyα wavelength shift varies from -3σ to -9σ. If we start with red Lyα photons, the final Lyα surface brightness profile becomes more compact. In Figure 9, the intrinsic Lyα luminosity for all curves is the same. The surface brightness curves for initially red photons appear to be of lower amplitude, because they have a central spike (within $0.02h^{-1}$Mpc) that is not shown in the left panel. The contribution of the central spike to the total luminosity can be figured out from the cumulative luminosity curves shown in the right panel. Overall, the Lyα emission appears to be close to point-like if photons start from the far red side of the line center. These red photons can still have a probability of experiencing resonant scatterings in the infall region around the halo and being shifted to

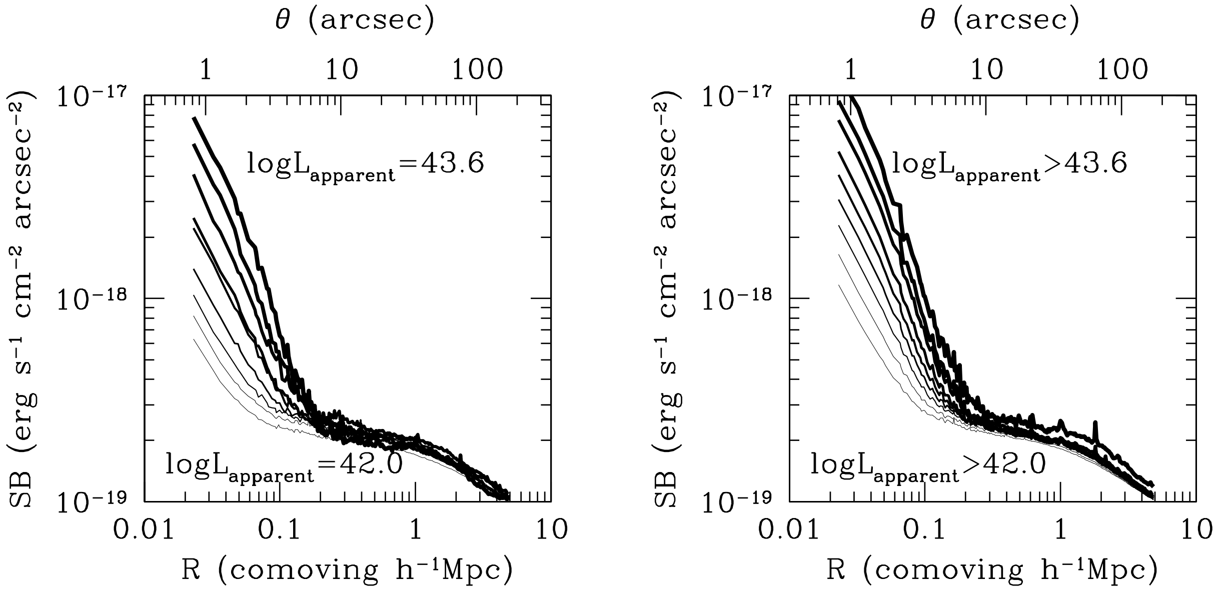

FIG. 8.— Dependence of mean Lyα surface brightness profile on the apparent (observed) Lyα luminosity. *Left:* Profiles for samples of galaxies in different bins of apparent Lyα luminosity. From bottom to top curves, apparent Lyα luminosity increases from $\log[L_{\rm apparent}/({\rm erg\,s^{-1}})] = 42.0$ to 43.6, with an interval of 0.2 dex between two adjacent curves. *Right:* Similar to the left panel, but for samples of galaxies above different thresholds in apparent Lyα luminosity.

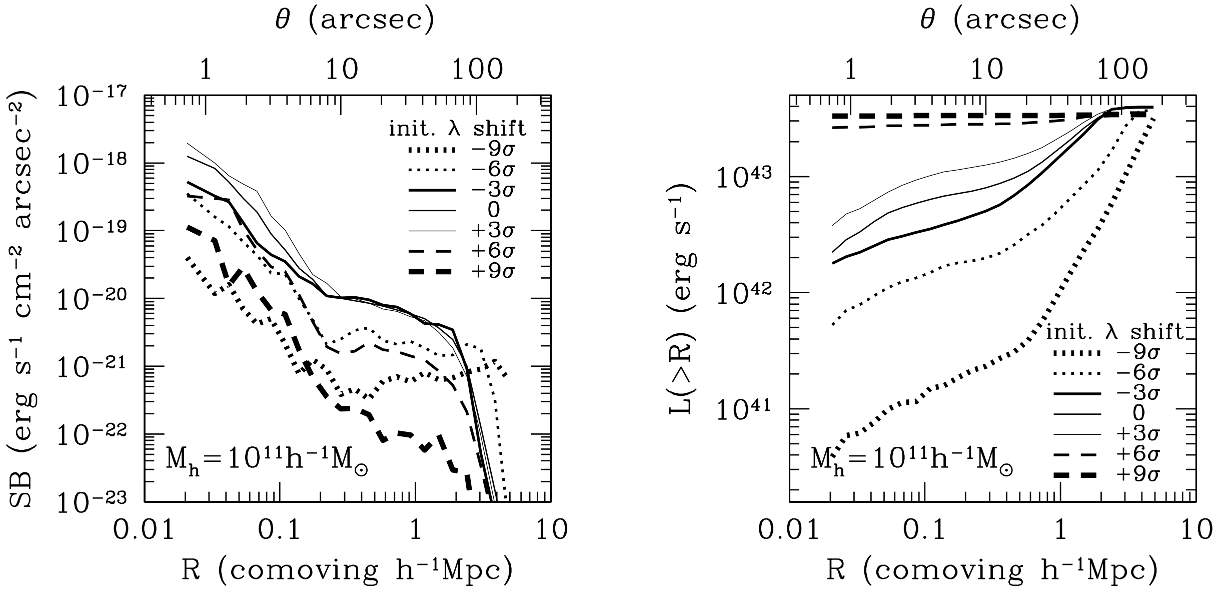

FIG. 9.— Dependence of Lyα emission distribution profile on initial wavelength of Lyα photons. The left and right panels are for the surface brightness profile and cumulative luminosity profile, respectively. For each curve, the initial Lyα photons are set to have a single wavelength, denoted in either panel as the difference from the line center in units of the 1D thermal width of the halo gas, which is about $\sigma = 69{\rm km\,s^{-1}}$ for $M_h = 10^{11}h^{-1}M_\odot$. The initial Ly$\alpha$ luminosity for all cases is normalized to be the same.

the blue side. The surface brightness profile on scales $\lesssim 1h^{-1}$Mpc is expected to be contributed by these photons. The probability of such scatterings depends on the magnitude of the shift and the infall velocity around the halo. For sources in $10^{11}h^{-1}M_\odot$ halos, even with a $+6\sigma$ initial line shift (thin dashed curves in Figure 9), the flattening part in the surface brightness profile can still be clearly seen (left panel), although the majority of the observed Lyα photons are from the central region (right panel). We verify that for a $+3.5\sigma$ initial line shift (not shown in the plot) the contribution from the central region to the total Lyα luminosity is $\lesssim$40%, less than that from the extended emission. If we take this as a threshold for the profile to change from point-like to extended, it would correspond to $\sim 250{\rm km\,s^{-1}}$.

If the wavelength shift of the initial Lyα photons is in the range of $\pm3\sigma$, the resultant surface brightness distribution is not sensitive to the initial Lyα wavelength, as shown by the solid curves in Figure 9. This is easy to understand: photons starting at a wavelength shift $\pm3\sigma$ undergo many scatterings in the core, leading to a distribution that loses memory of the original wavelength and to a nearly constant surface brightness profile. But photons with a larger initial wavelength deviation are not scattered enough times to be redistributed in this way before they escape. Therefore, the predicted Lyα profile should be reliable except when many photons are emitted from the central galaxy with a wavelength shift of several times the velocity dispersion.

To eliminate most of the extended Lyα emission around the galaxies, the initial line shifts (after photons escape the ISM) need to be larger than 250km s^{-1} for halos of $10^{11}h^{-1}M_{\odot}$. Galactic winds can have the effect of shifting Lyα emission toward red (e.g., Verhamme et al. 2006; Dijkstra & Wyithe 2010). From observations of $z \sim 3$ galaxies, Steidel et al. (2010) find that the interstellar absorption line shifts with respect to the Hα-defined galaxy systemic redshift by 165 ± 140km s^{-1} (mean $\pm$ standard deviation) for galaxies of baryon mass (stars plus cold gas) ranging from $\sim 1 \times 10^{10}M_{\odot}$ to $\sim 3 \times 10^{11}M_{\odot}$. The uncertainty of velocity measured for individual galaxies is estimated to be $\sim$ 130km s^{-1}. If the wind is confined in a region not far from the ISM, the above observational results indicate that the initial shift in Lyα emission could be above $\sim$ 300km s^{-1}. However, even in such a case, the shift may not be sufficient for Lyα photons to completely decouple from the circumgalactic and intergalactic environments, depending on the spatial distribution of the wind. Observationally, the outflowing neutral gas of the wind is not isotropic, usually collimated in a bipolar fashion (e.g., Bland & Tully 1988; Shopbell & Bland-Hawthorn 1998; Veilleux & Rupke 2002). It is likely that Lyα emission escaping in directions other than the wind would gain only a smaller redward shift, and the source would still become extended in the end. The wind effect on the spatial distribution of Lyα emission is also expected to be less significant for sources before reionization than those after reionization, since the higher neutral density boosts the scattering optical depth.

It is also possible that the wind could reach scales much larger than the ISM (e.g., Steidel et al. 2010). In such a case, the initial line shifts (after photons escape the ISM) is not much affected by the wind, but the wind alters the distribution and dynamics of neutral gas in the circumgalactic region and therefore the details in the Lyα radiative transfer process. While the surface brightness profile of Lyα emission may change accordingly, the extended Lyα emission should remain as a generic feature. Such a possibility deserves further investigations using high resolution galaxy formation simulations with a wind prescription.

A change in the initial Lyα line profile can lead to a change in the observed Lyα luminosity and therefore the observed Lyα luminosity function. However, as discussed in Paper I, a combination of changes in the star formation prescription used, the stellar IMF adopted, and the dust extinction is able to keep the predicted Lyα luminosity function to match the observed one. On the other hand, the change in the initial Lyα line profile can alter the strength of the coupling between the observed Lyα emission and the circumgalactic and intergalactic environments. This would show up in the clustering of LAEs (Paper II), which provides an interesting way to constrain the initial Lyα line profile and the effect of galactic wind.

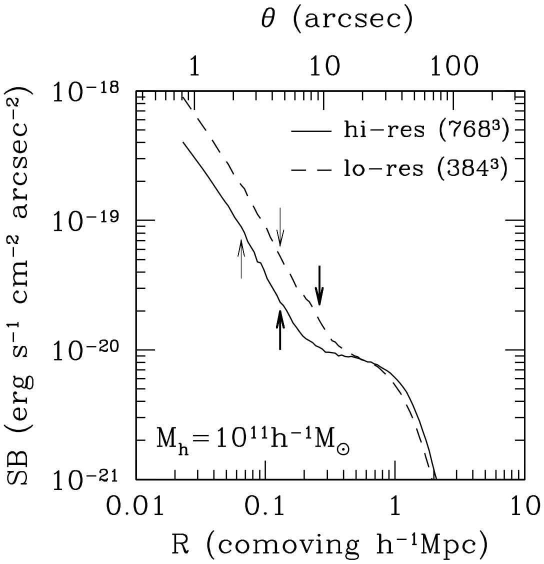

Fig. 10.— Effect of the resolution of the grid on the Lyα surface brightness profile. Shown here are average (one-halo term) profiles from stacking narrowband images of individual sources residing in halos of $10^{11}h^{-1}M_{\odot}$. The solid curve is obtained by performing Lyα radiative transfer calculation with gas properties (density, temperature, and peculiar velocity) represented with a 768^3 grid (default case in this paper), while the dashed curve shows the case with a lower resolution grid (384^3). For each case, the thin and thick arrows mark the half and full size of a grid cell, respectively. Note that the image pixels to collect Lyα photons is much finer than the grid cell. Calculation with the higher resolution grid tends to predict more extended Lyα emission.

2.5. *Effect of Grid Resolution*

For the main results in this paper, our Lyα radiative transfer calculation is performed in a 100^3h^{-3}Mpc^3 simulation box, where gas properties (density, temperature, and peculiar velocity) are sampled with a 768^3 grid. All Lyα photons are originally emitted from point sources and the scatterings of Lyα photons inside individual cells are also followed. As shown in Paper I, the dynamics of the infall region around halos plays a significant role in determining the distribution of Lyα photons, so we expect that the grid resolution in our calculation is able to predict the generic features in the extended Lyα emission. We perform a resolution test to show that this is the case.

It would be ideal to do such a test with a higher resolution grid. However, the available reionization simulation outputs prevent us from doing this. Therefore, we degrade the default 768^3 grid used in this paper to a lower resolution 384^3 grid by binning the gas density, temperature, and peculiar velocity. We then perform the Lyα radiative transfer calculation with such a grid for $10^{11}h^{-1}M_{\odot}$ halos and compare the resultant average Lyα surface brightness profile (the one-halo term) with that with the 768^3 grid.

The comparison is shown in Figure 10. For each resolution case, the thin and thick arrows mark the half and full size of a grid cell, respectively. For a source located at the center of a cell, the initial Lyα photons see a uniform gas distribution within a radius of about half cell size. However, the final Lyα surface brightness distribution inside this resolution radius is determined by the gas properties not only in this central cell but also in the surrounding cells. The reason is that Lyα photons propagating into surrounding cells have chances to be scattered back into the central cell. That is, the surface brightness profile is not a local quantity as a result of radiative transfer. Therefore, the small scale surface brightness profile (in particular the slope) is not completely a result of the grid resolution, as indicated by the fact that the powerlaw-like inner profile naturally extends to scales a few times larger than the resolution scale. The transition to a plateau is not an artifact of grid resolution, either.

With the low resolution grid, the general features in the Lyα surface brightness profile remain the same, a steep drop on small scales and an extended plateau on large scales before a sharp cutoff. However, the amplitude of the profile on small scales is about a factor of two higher with the low resolution grid, and it is compensated by a slightly lower amplitude on large scales. Therefore, a lower resolution has the effect of making the emission more concentrated.

If the grid were a factor of two finer than the default grid, we expect the predicted small scale surface brightness profile to be lower and the difference should be smaller than a factor of two. The Lyα emission would become *more* extended. We therefore expect that the generic prediction of the extended Lyα emission would be strengthened with an improved grid resolution.

Even though for the one-halo term of the surface brightness profile the overall cusp-to-plateau behavior does not depend on the grid resolution, the transition scale decreases for a higher resolution. Figure 10 seems to show that the transition happens at a scale about twice the cell size, indicating a resolution effect. Although cells around the source cell contribute to the determination of the profile of the central cusp, the cuspy profile itself is inevitably expected to also depend on the exact density, temperature, and velocity distributions of neutral gas within the source cell. The effects discussed in § 2.4 add further uncertainties in the cuspy profile.

Despite the above uncertainties, our prediction on the existence of the extended Lyα emission around high redshift star-forming galaxies remains valid, as long as Lyα photons encounter scatterings in the circum-galactic and inter-galactic media. The predicted two characteristic scales in the surface brightness profile from stacked images should also remain valid. The outer scale, which is mainly determined by the one-halo plateau region, is less sensitive to the exact central cuspy profile. The inner transition scale, on the other hand, depends on the amplitude and slope of the central cusp, which may not be properly resolved in our model. If the grid resolution is the only source of uncertainty, the inner transition scale of 0.1–0.2 Mpc (comoving) seen in the stacked profiles in § 2 should be regarded as upper limits.

3. DISCUSSION

The Lyα emission from star-forming galaxies is extended because of resonant scattering in the circumgalactic and intergalactic environments. In the stacked narrowband Lyα image, the change from a declining to nearly flat surface brightness profile at a characteristic scale of a few tenths of Mpc (possibly an upper limit, see § 2.5). and that from the flat profile to a declining profile at a few Mpc are evidence for the resonant scattering nature of the extended Lyα emission.

According to our radiative transfer modeling, the visibility of Lyα emission from star-forming galaxies depends on the circumgalactic and intergalactic environments around sources, and only the central, high surface brightness part can be detected as LAEs. The extended Lyα emission around the star-forming galaxies is predicted to exist (as long as Lyα photons escape from the ISM), no matter whether they can be detected as LAEs or not. This implies that the extended emission can be detected from both LBGs and LAEs. In practice, to detect the extended Lyα emission around LBGs, we need to know their redshifts and take their Lyα narrowband images. Extended Lyα emission from LAEs is more readily detected, since LAEs are typically discovered in narrowband surveys.

Our radiative transfer modeling is performed for $z=5.7$ star-forming galaxies. The generic picture should remain valid at other redshifts – as long as Lyα photons encounter significant scatterings in the circumgalactic/intergalactic media, the Lyα emission would become extended. However, the physical conditions in and around star-forming galaxies evolve with redshift. For example, compared to $z=5.7$ galaxies, we expect a lower neutral hydrogen density around $z\sim 3$ galaxies, as a result of the expansion of the universe and the evolution of the UV background. The Hubble expansion rate decreases, a change that may partially compensate the decrease in neutral density for Lyα scattering. The extended Lyα emission (e.g., the surface brightness profile) at $z\sim 3$ may not follow the details of our $z=5.7$ prediction, although it is expected to show up. We reserve the investigation of the redshift dependence of the extended Lyα emission for future work. We do not include dust in our model. The effect of ISM dust on the Lyα line depends on whether dust distribution is clumpy or not (Neufeld 1991; Hansen & Oh 2006). Optical, UV, and Lyα observations of local star-forming galaxies show evidence that ISM kinematics and geometry play a more significant role than dust in affecting the Lyα emission (e.g., Giavalisco et al. 1996; Keel 2005; Atek et al. 2008, 2009). We also expect the dust content to decrease towards high redshift (e.g., $z\sim 6$), and there is observational evidence for low dust content in $z\gtrsim 6$ galaxies (e.g., Bouwens et al. 2010; Ono et al. 2010). It is likely, however, that the existence of dust can lead to variations in the amount of Lyα photons escaping from the ISM, and thus add additional scatter in the extended Lyα emission among individual galaxies. Keeping all the above caveats in mind, we discuss the current status of observing the extended Lyα emission.

Observations have long been suggesting the existence of extended Lyα emission. Based on *Hubble Space Telescope (HST)* broad-band and *New Technology Telescope (NNT)* narrow-band images, Moller & Warren (1998) found that three LBG-like galaxies near a $z=2.8$ quasar are more extended in Lyα emission (half-light radius of $0.5''$–$0.7''$) than in the continuum (half-light radius of $0.13''$). Observations with NNT and Very Large Telescope (VLT) of a larger sample of LAEs (~ 70) in quasar fields at $z\sim 3$ further strengthen the case for extended Lyα emission (e.g., Fynbo et al. 2001, 2003; also see Laursen & Sommer-Larsen 2007 for comparing one of their objects with the results from a model with Lyα radiative transfer). In particular, Fynbo et al. (2001) found the size of Lyα emission to be $0.65''$ ($FWHM$) in the stacked narrow-band images of seven LAEs. Although the spatial extent of the Lyα emission from the above observations is small compared to what we predict, owing to the surface brightness detection limit, it is clear that Lyα emission is more extended than the underlying UV emission.

There are efforts to use stacked narrowband images in deep surveys to study the compactness of the Lyα emission. Hayashino et al. (2004) find that 24 spectroscopically confirmed $z \sim 3$ LBGs in Steidel et al. (2003) fall within the redshift range of their deep narrowband image observed with Subaru telescope (with only two of them being identified as LAEs). The UV luminosity of these LBGs ranges from -20 mag to -22.5 mag (based on the observed $\mathcal{R}_{\rm AB}$ magnitude; Steidel et al. 2003). After removing two gigantic Lyα blobs, the composite narrowband (continuum subtracted) image of the 22 LBGs shows Lyα emission that extends at least to $5''$ (about $0.1h^{-1}$Mpc comoving; see their Fig.8). The surface brightness drops from $\sim 3\times10^{-18}{\rm erg\,s^{-1}\,cm^{-2}\,arcsec^{-2}}$ at $\sim 1''$ to a few times $\sim 3\times10^{-19}{\rm erg\,s^{-1}\,cm^{-2}\,arcsec^{-2}}$ at $\sim 4''$, corresponding to a power-law index of ~ -1.7. They further note that 13 LBGs with no individual detection of extended Lyα emission also show extended Lyα emission on their composite image. The findings of Hayashino et al. (2004) are in line with our prediction that extended Lyα emission exists for LBGs, and the slope of the surface brightness profile is also in broad agreement with our prediction for UV bright sources.

Steidel et al. (2011) present the result of stacking analysis of deep narrow-band observation of 92 UV continuum-selected star-forming galaxies at $2.2 < z < 3.1$. [9] Some sources are the same ones as in Hayashino et al. (2004) but with much deeper narrow-band observation. The stacked narrowband image shows diffuse Lyα emission around star-forming galaxies, with surface brightness drops from a few $\times10^{-18}{\rm erg\,s^{-1}\,cm^{-2}\,arcsec^{-2}}$ at the center to $\sim 10^{-19}{\rm erg\,s^{-1}\,cm^{-2}\,arcsec^{-2}}$ at a radius of $\sim 10''$ ($\sim$80 proper kpc). The extended emission exists in the stacked image of sub-samples – LBGs, LAEs, and Lyα absorbers all show qualitatively similar diffuse emission. The overall surface brightness amplitude of the extended emission increases with the central Lyα emission. Although the redshift difference prevents us from a direct comparison between the observation and our prediction, the detected diffuse Lyα emission supports our generic picture that resonant scatterings in the circum-galactic and intergalactic media causes Lyα emission originated from star formation in the central galaxy to become extended. If we make a naive comparison, the Lyα emission is detected up to the inner characteristic scale in the surface brightness profile (e.g., Figures 7 and 8), not reaching the plateau yet. In Steidel et al. (2011), the clustered sources are intentionally masked before image stacking, which may change the shape of plateau if it could be detected. We plan to extend our model to $z \sim 3$ star-forming galaxies and make direct comparison with the observation in Steidel et al. (2011).

Ono et al. (2010) use stacked multiband images of LAEs at $z \sim$5.7 and 6.6 in the SXDS to investigate the stellar population of LAEs. For the narrowband stacked images, they find that the Lyα fluxes level off for apertures larger than $5''$ in diameter. Such a behavior in the surface brightness profile is predicted in our model as the transition to the two-halo term dominated regime. It is likely that the feature seen by Ono et al. (2010) is caused by the clustering of Lyα emitting sources.

Finkelstein et al. (2011) detect Lyα emission from three spectroscopically confirmed $z = 4.4$ LAEs in the HST/ACS F658N narrowband imaging data. They find that Lyα emission appears to be more extended than the UV emission. However, the half-light radii of Lyα emission are quite small, in the range of $0.1''$–$0.2''$. One thing to notice is that the observation is not deep enough to reach the sensitivity of detecting the much larger extended Lyα halo predicted by our model. This is clear from the fact that the surface brightness level in the *HST* narrowband observation turns out to be above a few times $10^{-16}{\rm erg\,s^{-1}\,cm^{-2}\,arcsec^{-2}}$. It is also supported by the fact that the three objects have significantly higher Lyα fluxes detected from ground-based narrowband image (with larger telescope apertures and reduced sensitivity to read noise; Finkelstein et al. 2011). With *HST*/WFPC2 narrowband images of eight $z = 3.1$ LAEs, Bond et al. (2010) find half-light radii of Lyα emission to be in a similar range, $0.15''$–$0.30''$. The surface brightness level (a few times $10^{-17}{\rm erg\,s^{-1}\,cm^{-2}\,arcsec^{-2}}$) reached by the observation is still too high to probe the extended Lyα emission predicted by our model.

Extended Lyα emission can also be detected through deep spectroscopic observations. Rauch et al. (2008) conduct a long-slit search for $2.67 < z < 3.75$ low surface brightness Lyα emission from a 92-hour long exposure with the VLT, reaching a 1σ surface brightness detection limit of $8\times10^{-20}{\rm erg\,s^{-1}\,cm^{-2}\,arcsec^{-2}}$ in a 1 arcsec^2 aperture. They find 27 objects with possible Lyα emission lines. These objects are typically fainter than the LAEs and LBGs in Steidel et al. (2011). About one third of them show clear signatures of extended emission. If the surface brightness profile at large radii is approximated by a power-law, the slope is generally in the range of -1 to -3 (their Figure 17). In the stacked surface brightness profile (their Figure 20), the emission clearly extends to $\gtrsim 4''$ (about comoving $90h^{-1}$kpc), dropping from $\sim 8\times10^{-19}{\rm erg\,s^{-1}\,cm^{-2}\,arcsec^{-2}}$ at a radius of $1''$to $\sim 1\times10^{-19}{\rm erg\,s^{-1}\,cm^{-2}\,arcsec^{-2}}$ at large radii. The profile roughly follows a power law with an index in the range of -1.5 to -2.0. This is in the ballpark of the predicted extended emission, although a direct comparison is not possible because of the redshift difference. The spatially resolved spectra of the extended emission remain as an interesting aspect to be explored in our model.

The extended Lyα halo from Lyα scatterings predicted by our model shares some similarities with the one around a quasar before reionization described in Loeb & Rybicki (1999). Unlike Loeb & Rybicki (1999), who assume a uniform, zero temperature IGM undergoing Hubble expansion, we use a realistic distribution of gas density, temperature, and velocity around a star-forming halo from cosmological reionization simulation. We expect that extended Lyα emission around star-forming galaxies also exists before reionization, which merits further study. However, the Lyα surface brightness is expected to be proportional to the source luminosity and to not depend on the neutral fraction in the IGM as long as the majority of photons are scattered, while it should decline with redshift as $(1+z)^{-4}$, making the detection increasingly difficult at higher redshift.

---

[9] It is exciting that our generic prediction (if dated from the initial submission of our paper) started to be tested or verified in merely three months, although many details remain to be investigated.

Our radiative transfer calculation is done for sources residing in halos above $5 \times 10^9 h^{-1} M_\odot$. Star formation in lower mass halos, down to $\sim 2 \times 10^8 h^{-1} M_\odot$ at $z \sim 5.7$ (with virial temperature $> 10^4 K$ for gas to cool; see Trac & Cen 2007), can also contribute to the two-halo term of the stacked profile. According to Trac & Cen (2007) (see their Fig.1), the total star formation rate in $< 5 \times 10^9 h^{-1} M_\odot$ halos can contribute about two thirds of the global rate. The amplitude of the clustering with these low mass halos is lower, and we expect that including the Lyα emission from the $< 5 \times 10^9 h^{-1} M_\odot$ halos would boost the two-halo term of the surface brightness profile presented in this paper at the factor of two level and that the two characteristic scales would shift inward. Our model does not resolve subhalos, but we do not expect a large subhalo (or satellite galaxy) fraction for galaxies at redshift $z \sim 6$. If we consider a mass threshold sample of halos with $M_h > M_{\rm min}$ and assume that the mean number of subhalos increase linearly with halo mass as $M_h/(10 M_{\rm min})$ (Kravtsov et al. 2004), we find that the satellite fraction is about 15% for $M_{\rm min} \sim 10^{11} h^{-1} M_\odot$. As subhalos are distributed inside virial radius of the parent halo, including star formation in subhalos would make the central cuspy surface brightness profile in the stacked image more extended, which would smooth the transition to the plateau part of the profile and increase the inner characteristic scale. Investigating the exact magnitude of the effect is beyond the scope of this paper.

Besides star formation, there are other sources of Lyα emission that increase in the dense regions around galaxies, including fluorescence from the UV background and cooling radiation. At $z \sim 5.7$, the fluorescent emission caused by the UV background is expected to be at the level of a few times $10^{-21} {\rm erg\, s^{-1}\, cm^{-2}\, arcsec^{-2}}$ (e.g., Gould & Weinberg 1996; Kollmeier et al. 2010), much fainter than the signal of interest in this paper. Cooling radiation may have a noticeable contribution to the stacked Lyα surface brightness profile, but there are uncertainties in the theoretical prediction (e.g., Faucher-Giguère et al. 2010). Further work is needed to see whether Lyα emission from cooling radiation can change the profile and to see how one can separate Lyα emission caused by star formation from other sources of Lyα emission.

Finally, for observational efforts, sky subtraction is an important step in revealing the extended Lyα emission from star-forming galaxies. To compare the observation with the theoretical prediction from simulations, a detailed description of the method of sky subtraction used in the observation is necessary, which should be reproduced in the same way in the model.

4. CONCLUSION

After escaping from the ISM, Lyα photons converted from ionizing photons in star-forming galaxies experience scatterings in the circumgalactic and intergalactic media. Such a radiative transfer process makes Lyα emission from these galaxies spatially extended. In this paper, built on the radiative transfer modeling of LAEs in Zheng et al. (2010) and Zheng et al. (2011), we investigate the predicted spatial distribution of Lyα emission that can be measured from the stacked narrowband image of these galaxies.

In general, the predicted surface brightness profile measured from the stacked image has two characteristic scales, an inner one at tenths of Mpc and an outer one at about 1 Mpc. The profile shows a central cusp inside the inner scale, an approximate plateau between the two scales, and an extended tail beyond the outer scale. The inner scale may possibly be an upper limit, as an effect of the grid resolution in the simulation (see § 2.5).

The stacked surface brightness profile can be understood as a superposition of the brightness distribution from the stacked sources themselves (one-halo term) and that from neighboring clustered sources (two-halo term). The two-halo term is the profile of the (angular) two-point correlation function (plus one) smoothed by the extended Lyα emission profile (PSF) of individual sources. The smoothing makes the profile flattened on scales smaller than the spatial extent of Lyα emission of clustered sources. The outer characteristic scale in the stacked surface brightness profile marks this spatial extent, and the plateau in the profile is a consequence of the smoothing effect. The transition from one-halo term domination to two-halo term domination leads to the inner characteristic scale seen in the stacked surface brightness profile.

For continuum selected galaxies (LBGs), the amplitude of the stacked Lyα surface brightness profile increases with the source UV luminosity (or halo mass) on both small and large scales. The two characteristic scales also increase with the UV luminosity. The central cusp becomes steeper for higher UV luminosity. For Lyα line selected galaxies (LAEs), the amplitude of the central cuspy profile increases with observed Lyα luminosity and the slope is steeper than that of LBGs. Beyond the inner characteristic scale, the amplitude of the surface brightness profile only has a weak dependence on observed Lyα luminosity. The inner and outer characteristic scales do not show strong dependence on Lyα luminosity, either.

Because of the contribution from source clustering to the stacked surface brightness profile, the cumulative Lyα luminosity from the stacked image does not converge to the intrinsic Lyα luminosity of the stacked sources. It is therefore not straightforward to estimate the total Lyα emission from the stacked image.

In detail, the surface brightness profile depends on the initial line profile of Lyα emission (after Lyα photons escape the ISM). The source would appear to be more compact in the narrowband image as the initial line shift toward red increases. If this shift is caused by galactic wind, the wind velocity needs to be comparable to a few times the virial velocity of the host halo and the wind needs to be largely isotropic to make Lyα emission point-like. Conversely, from the measured Lyα surface brightness profile in the narrowband image, it may be possible to constrain the effect of galactic winds. It is worth further study along this line.

Our particular prediction here is for sources after reionization is complete ($z \sim 5.7$). It is interesting to investigate how the prediction changes for star-forming galaxies at lower redshifts, because of the large amount of efforts in observing star-forming galaxies around redshift 2–4 (e.g., Rauch et al. 2008; Steidel et al. 2011) and in the local universe (e.g., Kunth et al. 2003; Hayes et al. 2007; Östlin et al. 2009). It is also necessary to study the extended emission for sources at higher redshifts, before reionization is complete, given the increasing observational efforts (e.g., Ouchi et al. 2010; Kashikawa et al. 2011).

At the time of our initial submission, we conclude that deep narrowband photometry from large ground-based telescopes is on the verge of detecting the extended Lyα emission around star-forming galaxies, including LBGs and LAEs (e.g., Hayashino et al. 2004; Ono et al. 2010). Now the latest observation by Steidel et al. (2011) indeed revealed the extended Lyα emission to large radii ($\sim 10''$) around LBGs and LAEs, starting to verify our prediction and provide stringent test to the theoretical model. The detection of the predicted Lyα emission supports the generic picture that Lyα radiative transfer in the circumgalactic and intergalactic environments produces extended Lyα emission. The extended Lyα emission opens a new window to study the circumgalactic and intergalactic environment of high-redshift star-forming galaxies. The surface brightness profile encodes information about cold baryons around galaxies, including their density, temperature, and velocity. All of these properties could be modified by galactic wind, so the extended emission in principle can put constraints on the galactic wind. The stacked Lyα image also includes contributions from faint galaxies that cannot be detected in a single exposure, which provides an opportunity to study low luminosity star-forming galaxies. The extended emission gives us a better idea on the total amount of Lyα emission from galaxies. When compared with the UV emission or other optically-thin line emission (e.g., Hα emission), we may infer the dust distribution and its effect on Lyα photons. With integral-field-units observations of high-redshift star-forming galaxies, we would have stacked spectra for the extended emission and expect to learn more about galaxy environments. Details on how to extract all the information encoded in the extended Lyα emission need to be investigated, and Lyα radiative transfer calculation, in combination with sophisticated models of star-forming galaxies and their environments, will play an irreplaceable role.

ZZ thanks Masami Ouchi, Tomoki Saito, and Chuck Steidel for helpful discussions and the hospitality of the Institute for the Physics and Mathematics of the Universe. We thank Andy Gould for useful comments and the referee for constructive suggestions. ZZ gratefully acknowledges support from Yale Center for Astronomy and Astrophysics through a YCAA fellowship. ZZ and DHW thank the Institute for Advanced Study for their hospitality during part of the work. RC acknowledges support from NASA grants NNG06GI09G and NNX08AH31G. JM is supported by the Spanish grant AYA2009-09745.

REFERENCES

Atek, H., Kunth, D., Hayes, M., Östlin, G., & Mas-Hesse, J. M. 2008, A&A, 488, 491
Atek, H., Schaerer, D., & Kunth, D. 2009, A&A, 502, 791
Berlind, A. A. & Weinberg, D. H. 2002, ApJ, 575, 587
Bland, J., & Tully, B. 1988, Nature, 334, 43
Bond, N. A., Feldmeier, J. J., Matković, A., Gronwall, C., Ciardullo, R., & Gawiser, E. 2010, ApJ, 716, L200
Bouwens, R. J., et al. 2010, ApJ, 708, L69,
Cooray, A., & Sheth, R. 2002, Phys. Rep., 372, 1
Cowie, L. L., & Hu, E. M. 1998, AJ, 115, 1319
Dijkstra, M., Lidz, A., & Wyithe, J. S. B. 2007, MNRAS, 377, 1175
Dijkstra, M., & Wyithe, J. S. B. 2010, MNRAS, 408, 352
Faucher-Giguère, C.-A., Kereš, D., Dijkstra, M., Hernquist, L., & Zaldarriaga, M. 2010, ApJ, 725, 633
Finkelstein, S. L., et al. 2011, ApJ, 735, 5
Fynbo, J. U., Möller, P., & Thomsen, B. 2001, A&A, 374, 443
Fynbo, J. P. U., Ledoux, C., Möller, P., Thomsen, B., & Burud, I. 2003, A&A, 407, 147
Gawiser, E., et al. 2007, ApJ, 671, 278
Giavalisco, M., Koratkar, A., & Calzetti, D. 1996, ApJ, 466, 831
Gould, A., & Weinberg, D. H. 1996, ApJ, 468, 462
Guaita, L., et al. 2010, ApJ, 714, 255
Hansen, M., & Oh, S. P. 2006, MNRAS, 367, 979
Hayashino, T., et al. 2004, AJ, 128, 2073
Hayes, M., Östlin, G., Atek, H., Kunth, D., Mas-Hesse, J. M., Leitherer, C., Jiménez-Bailón, E., & Adamo, A. 2007, MNRAS, 382, 1465
Hu, E., & McMahon, R. G. 1996, Nature, 382, 281
Kashikawa, N., et al. 2011, ApJ, 734, 119
Keel, W. C. 2005, AJ, 129, 1863
Kollmeier, J. A., Zheng, Z., Davé, R., Gould, A., Katz, N., Miralda-Escudé, J., & Weinberg, D. H. 2010, ApJ, 708, 1048
Kravtsov, A. V., Berlind, A. A., Wechsler, R. H., Klypin, A. A., Gottlöber, S., Allgood, B., & Primack, J. R. 2004, ApJ, 609, 35
Kunth, D., Leitherer, C., Mas-Hesse, J. M., Östlin, G., & Petrosian, A. 2003, ApJ, 597, 263
Laursen, P., & Sommer-Larsen, J. 2007, ApJ, 657, L69
Loeb, A., & Rybicki, G. B. 1999, ApJ, 524, 527
Madau, P., Pozzetti, L., & Dickinson, M. 1998, ApJ, 498, 106
Malhotra, S., & Rhoads, J. 2004, ApJ, 617, L5
Moller, P., & Warren, S. J. 1998, MNRAS, 299, 661
Neufeld, D. A. 1991, ApJ, 370, L85
Ono, Y., Ouchi, M., Shimasaku, K., Dunlop, J., Farrah, D., McLure, R., & Okamura, S. 2010, ApJ, 724, 1524
Östlin, G., Hayes, M., Kunth, D., Mas-Hesse, J. M., Leitherer, C., Petrosian, A., & Atek, H. 2009, AJ, 138, 923
Ouchi, M., et al. 2008, ApJS, 176, 301
Ouchi, M., et al. 2010, ApJ, 723, 869
Partridge, R.B., & Peebles, P.J.E. 1967, ApJ, 147, 868
Pieri, M. M., Frank, S., Weinberg, D. H., Mathur, S., & York, D. G. 2010, ApJ, 724, L69
Rauch, M., et al. 2008, ApJ, 681, 856
Rhoads, J. E., et al. 2003, AJ, 125, 1006
Seljak, U. 2000, MNRAS, 318, 203
Shopbell, P. L., & Bland-Hawthorn, J. 1998, ApJ, 493, 129
Steidel, C. C., Adelberger, K. L., Shapley, A. E., Pettini, M., Dickinson, M., & Giavalisco, M. 2003, ApJ, 592, 728
Steidel, C. C., Erb, D. K., Shapley, A. E., Pettini, M., Reddy, N., Bogosavljević, M., Rudie, G. C., & Rakic, O. 2010, ApJ, 717, 289
Steidel, C. C., Bogosavljević, M., Shapley, A. E., Kollmeier, J. A., Reddy, N. A., Erb, D. K., & Pettini, M. 2011, in press, arXiv:1101.2204
Taniguchi, Y., et al. 2009, ApJ, 701, 915
Trac, H., & Cen, R. 2007, ApJ, 671, 1
Trac, H., Cen, R., & Loeb, A. 2008, ApJ, 689, L81
Veilleux, S., & Rupke, D. S. 2002, ApJ, 565, L63
Verhamme, A., Schaerer, D., & Maselli, A. 2006, A&A, 460, 397

Wang, J.-X., Malhotra, S., Rhoads, J. E., Zhang, H.-T., & Finkelstein, S. L. 2009, ApJ, 706, 762

Zheng, Z., Cen, R., Trac, H., & Miralda-Escude, J. 2010, ApJ, 716, 574

Zheng, Z., Cen, R., Trac, H., & Miralda-Escude, J. 2011, ApJ, 726, 38